Research Article

Pt nanoparticles supported on nitrogen-doped porous carbon as efficient oxygen reduction catalysts synthesized via a simple alcohol reduction method

Naoki Tachibana[1] · Yasuyuki Yukawa[1] · Kazuo Morikawa[1] · Masahiro Kawaguchi[1] · Kengo Shimanoe[2]

Received: 3 December 2020 / Accepted: 4 February 2021 / Published online: 17 February 2021

Abstract
Pt nanoparticles supported on nitrogen-doped porous carbon (NPC) were investigated as both a highly active catalyst for the oxygen reduction reaction (ORR) and a suitable porous support structure. Pt/NPC catalysts with loadings of 8.8–35.4 wt.% were prepared via a simple alcohol reduction method and exhibited homogeneously dispersed Pt nanoparticles with a small mean size ranging from 1.90 to 2.99 nm. X-ray photoelectron spectroscopy measurement suggested the presence of strong interactions between the Pt nanoparticles and NPC support. 27.4% Pt/NPC demonstrated high catalytic activity for the ORR in a rotating disk electrode system and was also effectively applied to a gas diffusion electrode (GDE). A GDE fabricated using the Pt/NPC with a fine pore network exhibited excellent performance, especially at high current densities. Specific activity of Pt/NPC and Pt/carbon black catalysts for the ORR correlated with the peak potential of adsorbed OH reduction on Pt, which was dependent on the particle size and support.

Supplementary information The online version contains supplementary material available at https://doi.org/10.1007/s42452-021-04343-8

✉ Naoki Tachibana, tachibana.naoki@iri-tokyo.jp | [1]Tokyo Metropolitan Industrial Technology Research Institute, 2-4-10, Aomi, Koto-ku, Tokyo 135-0064, Japan. [2]Department of Advanced Materials Science and Engineering, Faculty of Engineering Sciences, Kyushu University, 6-1, Kasugakoen, Kasuga-shi, Fukuoka 816-8580, Japan.

Graphic abstract

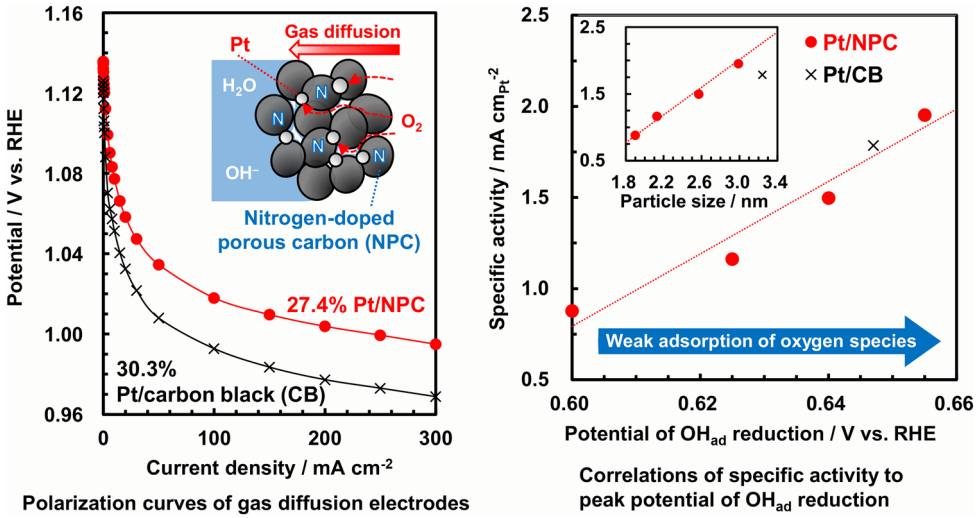

Keywords Oxygen reduction · Pt nanoparticles · Nitrogen-doped carbon · Porous carbon

1 Introduction

Electrocatalysts for the oxygen reduction reaction (ORR) in alkaline media have attracted tremendous interest for their applications in alkaline fuel cells [1–4], metal–air batteries [5, 6], and chlor-alkali electrolysis with oxygen depolarized cathodes [7]. Recently, alkaline membrane fuel cells, which can be simplified and the CO_2 poisoning problem for alkaline fuel cells is alleviated [8], have been reported to exhibit improved performance, which approaches that of proton exchange membrane fuel cells, due to advances in anion-exchange membranes [9]. At present, Pt and Pt-alloy nanoparticles supported on carbon are universally available electrocatalysts for the ORR [10, 11]. Among carbon support materials, carbon blacks (CBs) are commonly used in gas diffusion electrodes (GDEs) for fuel cells and metal–air batteries because of their large surface area, good electric conductivity, and well-developed porous structure as well as low cost [12, 13]. Despite these advantages, the slow kinetics of CB-supported Pt nanoparticles for the ORR necessitates high loading levels of Pt, hindering the further deployment of the electrochemical energy conversion and storage devices.

In order to improve the performance of Pt nanoparticle catalysts, decreasing the particle size and thereby increasing the surface area per unit mass is one of the reasonable strategies in heterogeneous catalyst fields [14]. However, many reports have demonstrated that the specific activity (current density per unit surface area) of Pt nanoparticles for the ORR decreases with decreasing particle size between about 1 and 5 nm and mass activity (current density per unit mass) does not linearly increase in this size range [15–17]. The effects of small Pt size on the ORR activity may be predicted by considering the ratio of terrace, corner, and edge sites on the particles [18, 19]. Following the geometrical considerations, the distribution of the surface sites rapidly changes for the small nanoparticles, which may lead to the strong adsorption of oxygen species, such as OH and O, through an increased number of low-coordinated sites [20, 21]. The strongly adsorbed species on the surface inhibit the adsorption of molecular oxygen and intermediates for the ORR [22]. Thus, the state and coverage of the oxygen species is considered to be a key factor in determining the activity of Pt catalysts [13, 23, 24]. Besides, it is suggested that the ORR activity of Pt nanoparticle catalysts can be related to interparticle distances and mass transport of oxygen [25, 26]. Watanabe et al. have reported that, if the Pt interparticle distance is too close (< 20 nm), the diffusion field of the particles for O_2 overlaps, resulting in decreased specific activity for the ORR [25].

It is widely recognized that support materials can significantly affect the catalytic activity of Pt nanoparticles [27–29]. Therefore, long-running efforts to develop various supports such as graphene [30, 31], carbon nanotubes [32, 33], CBs [34, 35], metal carbides [36, 37], and metal oxides [38] have been undertaken. Carbon supports with high graphitic nature have both excellent electrical conductivity and high mechanical strength, but the carbon lattice with strong sp^2 chemical bonds does not readily

permit the chemisorption of Pt on the basal planes [39]. Because nitrogen doping can introduce anchoring sites for Pt deposition, nitrogen-doped carbon has been used as a support for Pt catalysts over the past few decades [40–43]. Furthermore, it is suggested that surface nitrogen species such as pyridinic N in nitrogen-doped carbon increase the interactions between Pt catalysts and nitrogen-doped carbon supports, which may enhance the catalytic performance [42, 44, 45]. Nitrogen-doped porous carbon (NPC) supports with large surface area and high pore volume, which can act as a substrate for the effective dispersion of Pt nanoparticles and facilitate mass transport, would contribute to improving the ORR activity of Pt nanoparticles.

In the present study, Pt nanoparticles supported on NPC were prepared via a surfactant-free alcohol reduction method and characterized by transmission electron microscopy (TEM), X-ray photoelectron spectroscopy (XPS), X-ray diffraction (XRD), scanning electron microscopy (SEM), and N_2 gas adsorption. To evaluate the ORR activity, rotating disk electrode (RDE) measurements were conducted on the synthesized catalysts. Furthermore, a GDE was fabricated using Pt/NPC as an ORR catalyst and exhibited excellent performance, especially at high current densities.

2 Experimental section

2.1 Preparation of Pt nanoparticles supported on nitrogen-doped porous carbon

NPC was prepared via heat treatment using commercial CB (Ketjen Black EC600JD, Lion) and cyanamide (Sigma-Aldrich), which were used as carbon and nitrogen sources, respectively (for full details, see supplementary material) [46]. Pt nanoparticles supported on NPC were synthesized via an alcohol reduction process [47, 48] using dinitrodiamine platinum as a platinum source and methanol as a solvent and reducing agent. In a typical procedure, 100 mg of NPC with a nitric acid solution of dinitrodiamine platinum (Kojima Chemicals) was suspended by sonication in 10 mL of methanol for 10 min. The Pt loading was controlled by varying the amount of dinitro-diamine platinum. The mixtures were then heated to reflux under N_2 flow for 6 h in a round-bottom flask equipped with a condenser, thermal controller, and magnetic stirring bar. The reduction process was monitored by observing the color changes in the solution; from the original transparent yellow to colorless (Fig. S1a, b). In addition, the UV–Vis absorption spectra of the solutions were measured using a UV–Vis–NIR spectrophotometer (UV-3600, Shimadzu). The absorbance in wavelengths lower than 470 nm with a shoulder at 260 nm of dinitrodiamine platinum solution was not observed in the spectra for the solution after 6 h of methanol reduction (Fig. S1c). After the mixtures cooled, the solid precipitates were filtered, washed thoroughly with ethanol and distilled water, and then fully dried at 40 °C for 12 h. Pt nanoparticles supported on CB as reference catalysts were prepared in the same manner.

2.2 Material characterization

The Pt content in the synthesized catalysts was confirmed by inductively coupled plasma atomic emission spectroscopy (SPECTRO ARCOS, SPECTRO). The morphology of samples was observed by TEM (Titan Cubed G2 60–300, FEI Company) and SEM (SU-8220, Hitachi High-Technologies). The sample powders for TEM measurements were suspended in ethanol and dropped onto holey carbon films supported by Cu microgrids. The interparticle distance was calculated by

$$X = (1/3)[(3)^{0.5}\pi\sigma d^3 S(100 - y)/y]^{0.5} \quad (1)$$

where X is the interparticle distance in nm, σ is density of catalyst particles in g nm^{-3}, d is mean size of catalyst particles in nm, S is specific surface area of supports in nm^2 g^{-1}, and y is catalyst content in wt.% [25, 49]. XPS (Quantera SXM, Ulvac-phi) was performed using an Al Kα X-ray source (1486.6 eV). The peak shift correction was based on the binding energies of Cu 2p at 932.62 eV and Au 4f at 83.96 eV. Sample powders for XPS measurements were uniformly pressed onto an indium plate (Nilaco). Fitting of the N 1 s peak was performed using four common bonding configurations within the carbon lattice, including pyridinic N, pyrrolic N, quaternary N, and oxidized N [50]. The Pt 4f peak was fitted using the $4f_{7/2}$ and $4f_{5/2}$ components, which were separated by 3.3 eV with a fixed area ratio of 4/3 [51]. XRD patterns were obtained using an X-ray diffractometer (X'Pert Pro, Spectris) with a Cu Kα radiation source operated at 45 kV and 35 mA. The crystallite size of Pt in nm was calculated using the Scherrer's equation:

$$L = K\lambda/\beta\cos\theta \quad (2)$$

where L is the crystallite size in nm, K is the dimensionless shape factor (0.9), λ is the wavelength of Cu Kα radiation (0.154 nm), β is the full-width half-maximum of Pt (220) peaks in radians, and θ is the angle at the position of the peak maximum in radians [52]. Raman data were collected using a confocal Raman microscope (InVia Reflex, Renishaw) with a 532 nm laser as the excitation source. N_2 adsorption/desorption isotherms were obtained using a surface area and pore size distribution analyzer (BELSORP-max, Nihon BEL). The pore size distribution was estimated on the basis of the Barrett–Joyner–Halenda

(BJH) model [53]. Specific surface area was calculated from the Brunauer–Emmett–Teller (BET) equation in the partial pressure range of 0.05 – 0.20 N_2 [54]. The micropore volume was determined from the intercept of the *t*-plot [55]. The total pore volumes were obtained from the total adsorbed gas amount at a partial pressure of 0.98. The conversion factor from the amount adsorbed to the volume of liquid adsorbate was 0.0015468 under the assumption that the density of the condensed adsorbate in the pores is equal to the density of the bulk liquid adsorbate [56].

2.3 Electrochemical characterization

Electrochemical measurements were performed using a RDE and a GDE. All water used was first purified by a Barnstead Nanopure Diamond System (18.2 MΩ cm resistivity). Potentials were *i*R-corrected to compensate for the effect of solution resistance. Working RDEs (0.196 cm^2 geometrical surface area) were prepared as follows: initially, 5.0 mg of a catalyst sample was dispersed in 2-propanol solvent (Wako Chemical) with 50 µL of a 5.0 wt.% Nafion solution (Sigma-Aldrich). The mixture (5.0 mg mL^{-1}) was agitated ultrasonically for 30 min in an ice bath to form a uniform catalyst ink. The suspension (3.3 µL) was deposited in increments of 1.1 µL onto the electrode on an inverted rotator shaft (gently spinning at 0–100 rpm) and dried while spinning at ~ 100 rpm in air at room temperature for ~ 5 min, producing Pt loadings on the RDEs of 7.4–29.8 μg_{Pt} cm^{-2} for the catalysts with Pt concentrations of 8.8–35.4 wt.%. The catalyst-deposited electrode was further dried at 60 °C for 30 min to fully remove the 2-propanol. Electrochemical measurements were conducted using a potentiostat (HZ-5000, Hokuto Denko) with a three-electrode cell system. The reference electrode was an Hg/HgO electrode (KOH, 0.1 M), the counter electrode was a platinum wire, and the electrolyte was 0.1 M KOH solution. Before electrochemical measurements, ~ 100 cycles of cyclic voltammetry were performed by scanning the potential between 0.3 and – 0.8 V vs. Hg/HgO at a sweep rate of 0.5 V s^{-1} in a N_2-saturated electrolyte to clean the surfaces of the catalysts. The background currents were measured at a sweep rate of 20 mV s^{-1} in the N_2-saturated electrolyte. After the background current was measured, the electrolyte was saturated for more than 30 min with O_2. Linear sweep voltammograms were recorded at a sweep rate of 20 mV s^{-1} at 25 °C, and the oxygen reduction current was corrected by the background current. For the Tafel plot, the kinetic current density (j_k) was calculated from a mass-transport correction of the RDE by

$$j_k = j \times j_l / (j_l - j) \quad (3)$$

where *j* is the disk current density after correction for background current and j_l is the diffusion-limiting current density [57, 58]. Mass and specific activities were estimated via calculation of the kinetic current and normalization to the Pt loading and electrochemical surface area, respectively. The electrochemical surface area was calculated using Eq. (4) on the basis of the hydrogen adsorption charge in the negative potential scan from 0.40 to 0.05 V vs. RHE at a sweep rate of 20 mV s^{-1} on cyclic voltammograms after the current at 0.40 V was subtracted from the total current to correct for double-layer charging.

$$\text{Electrochemical surface area} = Q_H / W_{Pt} \times 0.21 \quad (4)$$

where Q_H is the measured hydrogen charge, W_{Pt} is the loading of Pt, and 0.21 mC cm^{-2} is the charge required to oxidize a monolayer of hydrogen on the Pt sites [57, 59]. Because the current at ~ 0.4 V includes a significant contribution from the surface (100) terrace domains on the Pt nanoparticles in alkaline solution, the electrochemical surface area of the synthesized catalysts was determined in 0.1 M $HClO_4$ in order to avoid overestimating the double-layer charging [60, 61].

Polarization curves of the GDEs with incorporated catalysts were obtained galvanostatically. The GDEs were fabricated using a previously reported procedure [62]. The GDE (diameter = 14 mm) comprised a catalyst layer (about 0.1 mm thick) and a gas diffusion layer (about 0.1 mm thick) formed on a Ni mesh current collector (100 mesh, Nilaco). The sample powder, a polytetrafluoroethylene (PTFE) dispersion (D-210C, Daikin Industries), and 1-butanol (Kishida Chemical) were added to distilled water and agitated ultrasonically for 30 min. The PTFE content in the catalysts was fixed at 30 wt.%. After filtration and drying at 125 °C, a powder was obtained for the catalyst layer. The powder for the gas diffusion layer was fabricated separately by mixing acetylene black (mean diameter = 48 nm; HS-100, Denki Kagaku Kogyo), a PTFE dispersion, and Triton-X surfactant (Kishida Chemical) in distilled water. The PTFE content of this powder was also fixed at 30 wt.%. After the mixture was filtered and dried at 125 °C, the obtained powder was heated at 280 °C for 3 h in an electric furnace to remove the surfactant. The powders for both layers and the Ni mesh were hot-pressed at 360 °C to produce the GDEs. The steady-state current density–potential curves of the PTFE cells installed with the fabricated GDEs were measured in 8 M KOH at 65 °C under O_2 flow (100 mL min^{-1}) using a Pt-mesh counter electrode and a double-junction Hg/HgO reference electrode (KOH, 8 M). Potentials versus Hg/HgO were converted to the RHE scale according to $V_{\text{vs. RHE}} = V_{\text{measured vs. Hg/HgO}} + 0.098 + 0.059 \times \text{pH}_{\text{electrolyte}}$ (pH = 13.0 for 0.1 M KOH, pH = 15.3 for 8 M KOH).

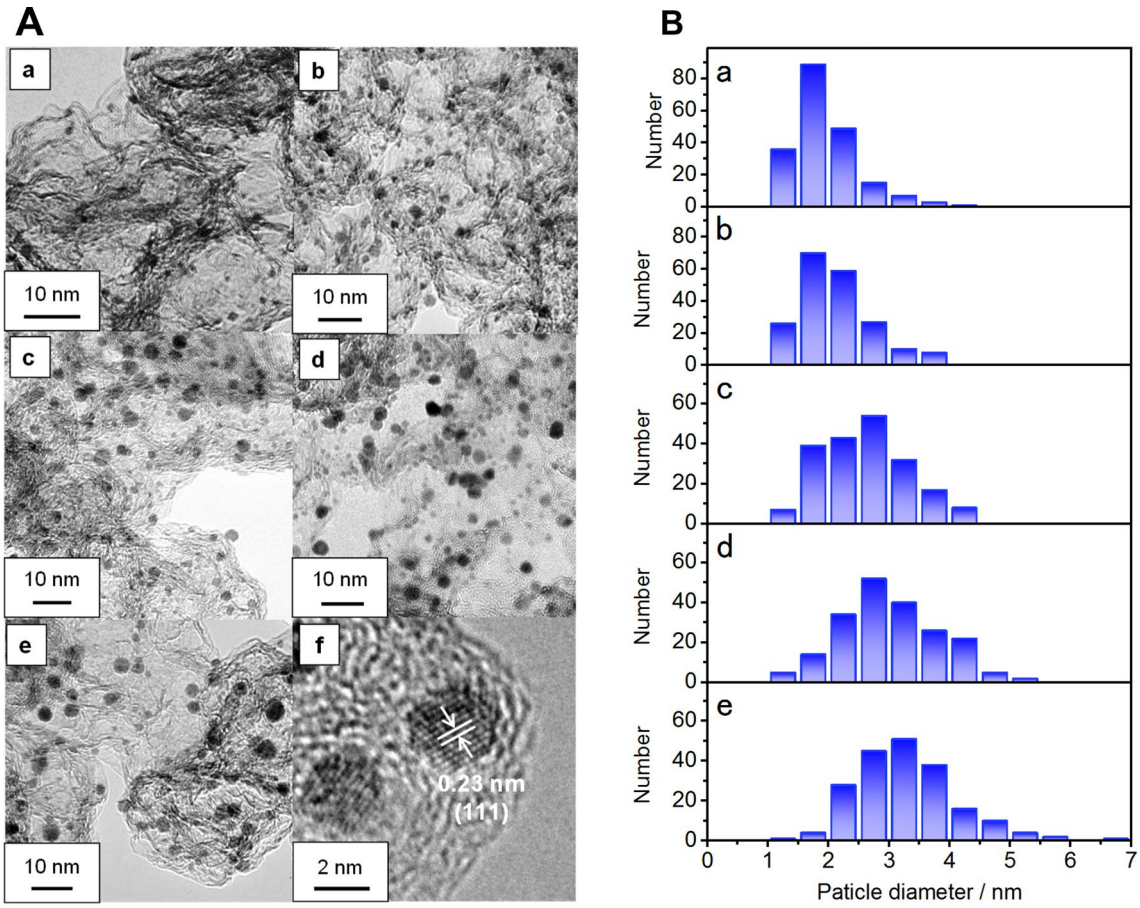

Fig. 1 **A** TEM images and **B** particle size distributions of *a* 8.8% Pt/NPC, *b* 19.6% Pt/NPC, *c*, *f* 27.4% Pt/NPC, *d* 35.4% Pt/NPC, and *e* 30.3% Pt/CB

Table 1 Mean particle size, crystallite size, and interparticle distance of Pt/NPCs and 30.3% Pt/CB

	Mean particle size/nm	Crystallite size/nm	Interparticle distance/nm
8.8% Pt/NPC	1.90 ± 0.54	–	27.8
19.6% Pt/NPC	2.13 ± 0.59	2.11	22.6
27.4% Pt/NPC	2.57 ± 0.70	2.48	24.1
35.4% Pt/NPC	2.99 ± 0.81	2.82	25.1
30.3% Pt/CB	3.24 ± 0.83	3.14	32.0

3 Results and discussion

3.1 Material characterization of Pt nanoparticles supported on nitrogen-doped porous carbon

To determine the mean size of the Pt nanoparticles in synthesized catalysts, they were characterized by TEM (Fig. 1). Pt nanoparticles were uniformly dispersed on the NPC support with a loading of 8.8–35.4 wt%, yielding a mean size in the range from 1.90 to 2.99 nm (Table 1). The mean sizes of the Pt/NPCs increased with increasing loading. Meanwhile, 30.3% Pt/CB exhibited a larger mean size of 3.24 nm than 35.4% Pt/NPC (mean size: 2.99 nm). The high-resolution TEM image of 27.4% Pt/NPC (Fig. 1f) shows clear lattice fringes throughout the particles, with a distance of 0.23 nm, which is consistent with the *d*-spacing of (111) planes of face-centered-cubic Pt, corroborating that the nanoparticles are Pt nanocrystals. Figure 2A, B and Table 2 show the C 1 *s* and N 1 *s* XPS spectra and atomic concentrations of NPC and CB supports. The XPS overview spectra of Pt/NPCs, Pt/CB, NPC, and CB are shown in Fig. S2. The C 1 *s* peak of sp^2 carbon at 284.5 eV for NPC is asymmetric and broad toward the high-binding-energy side due to the presence of C–N, C–O, C=O, O=C–O, and plasmon bands [63, 64]. Nitrogen atoms serve to mediate the enhancement in the strong adsorption of Pt by activating nitrogen-neighboring carbon atoms [65, 66]. Such activation can facilitate nucleation and subsequent particle growth. The increased number of nucleation sites

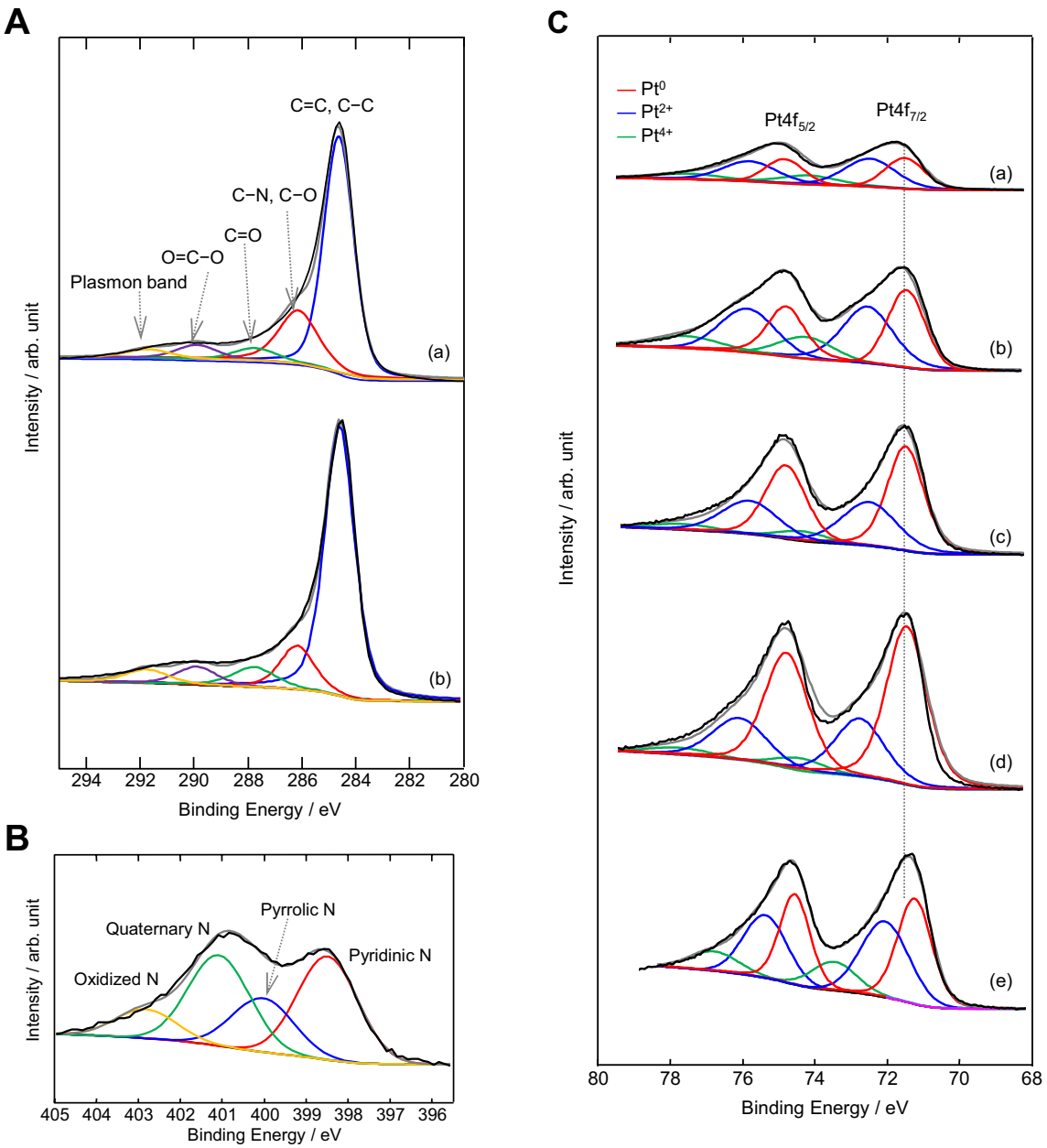

Fig. 2 **A** C 1 *s* XPS spectra of *a* NPC and *b* CB. **B** N 1 *s* XPS spectra of NPC. **C** Pt 4*f* XPS spectra of *a* 8.8% Pt/NPC, *b* 19.6% Pt/NPC, *c* 27.4% Pt/NPC, *d* 35.4% Pt/NPC, and *e* 30.3% Pt/CB

Table 2 Surface concentration of NPC and CB measured by XPS

	C 1 *s* / at.%	O 1 *s* / at.%	N 1 *s* / at.%
NPC	96.72	2.50	0.78
CB	97.17	2.83	–

provided by nitrogen atoms would result in small mean sizes of Pt nanoparticles on the NPC support. The interparticle distance of Pt/NPCs with small mean particle sizes was narrow compared with that of 30.3% Pt/CB (Table 1), suggesting that a large number of the nucleation sites were present on the NPC. Figure 2C shows the Pt 4*f* XPS spectra of the Pt/NPCs and 30.3% Pt/CB. The Pt 4*f* spectra can be deconvoluted into three pairs of doublets attributable to metallic Pt (Pt^0), Pt^{2+}, and Pt^{4+}. The binding energy of the Pt^0 $4f_{7/2}$ peak of ~ 71.5 eV for the Pt/NPCs was shifted from 71.2 eV for 30.3% Pt/CB, suggesting the presence of strong interactions between Pt nanoparticles and NPC support in the Pt/NPCs. The up-shift would result from the electronic structure modified by NPC support, which may result in the downshift of the *d*-band center position

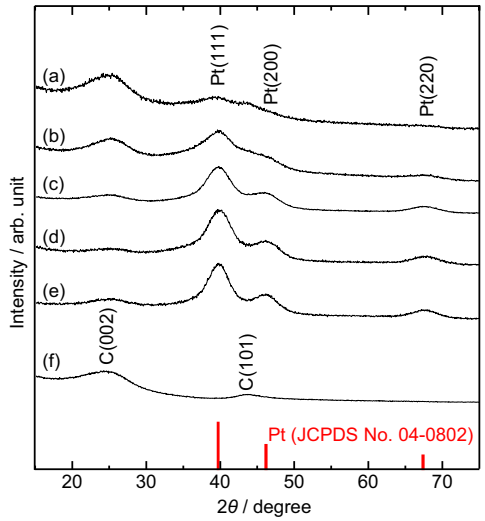

Fig. 3 XRD patterns of **a** 8.8% Pt/NPC, **b** 19.6% Pt/NPC, **c** 27.4% Pt/NPC, **d** 35.4% Pt/NPC, **e** 30.3% Pt/CB, and **f** NPC

[67, 68]. First-principles study revealed that Pt nucleation is favorable on pyridinic and pyrrolic N, and the center of *d*-band can be shifted downward by the nitrogen species [69]. Thus, the species on the NPC could be attributed to the increase in interactions between the Pt nanoparticles and NPC support. The interactions would enhance adhesion of the Pt nanoparticles to the NPC support [70], which could alleviate the aggregation of the nanoparticles.

The XRD spectra of the Pt/NPCs, 30.3% Pt/CB, and NPC are shown in Fig. 3. Two broad peaks for NPC were observed at about 24.5° and 43.5°, corresponding to the (002) and (101) diffraction peaks of hexagonal graphitic carbon (JCPDS No. 75–1621). The broad (002) basal plane peak indicates that the NPC comprises small crystalline structures. The diffraction peaks of the face-centered-cubic Pt can be identified from the spectral database (JCPDS No. 04–0802). The crystallite sizes of the Pt in 19.6% Pt/NPC, 27.4% Pt/NPC, 35.4% Pt/NPC, and 30.3% Pt/CB were calculated to be 2.11, 2.48, 2.82, and 3.14 nm, respectively, from the (220) peaks using Scherrer's equation. The increase in the crystallite size of the Pt/NPCs with increasing Pt loading is consistent with the increasing trend of the mean particle sizes revealed by TEM. The mean particle size of 2.13 nm for 19.6% Pt/NPC was almost the same as the crystalline size of 2.11 nm, indicating that the Pt nanoparticles were monocrystalline. However, the mean particle size of 2.57 and 2.99 nm for 27.4% and 35.4% Pt/NPCs were slightly larger than the crystalline sizes of 2.48 and 2.82 nm, respectively, suggesting that some Pt nanoparticles were aggregated on the NPC support. The interparticle distance of the Pt/NPCs increased from 22.6 to 25.1 nm as the loading increased from 19.6% to 35.4%, suggesting a decrease in the number of particles on the NPC, which can be attributed to the slight aggregation of the nanoparticles.

Figs. S3, and S4 show SEM images and Raman spectra of 27.4% Pt/NPC, 30.3% Pt/CB, NPC, and CB. The Raman spectra consist of two dominant peaks assigned to the first order G and D modes. The G mode has E_{2g} symmetry and is attibuted to the inplane stretching vibration of carbon atom pairs [71]. The D mode has A_{1g} symmetry and is attributed to the inplane breathing vibration of the six-membered aromatic carbon rings [71]. The two additional broad peaks around 1200 and 1515 cm^{-1} correspond to the disordered graphite similar to polyaromatic hydrocarbons and a graphitic layer containing distorted structures such as integrated heteroatoms [72, 73]. The size of NPC primary particles and intensity ratio of D (disorder) and G (graphite) bands, I_D/I_G, for 27.4% Pt/NPC and those for NPC were found to be nearly identical: about 30 nm and 1.34, respectively, and the deposition of Pt nanoparticles on NPC did not significantly affect

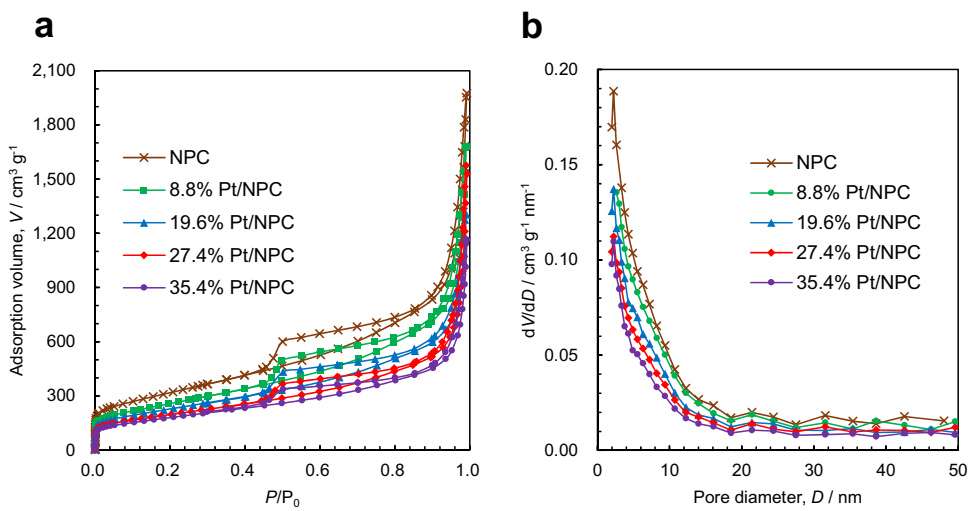

Fig. 4 **a** N_2 adsorption/desorption isotherms and **b** pore size distributions of Pt/NPCs and NPC

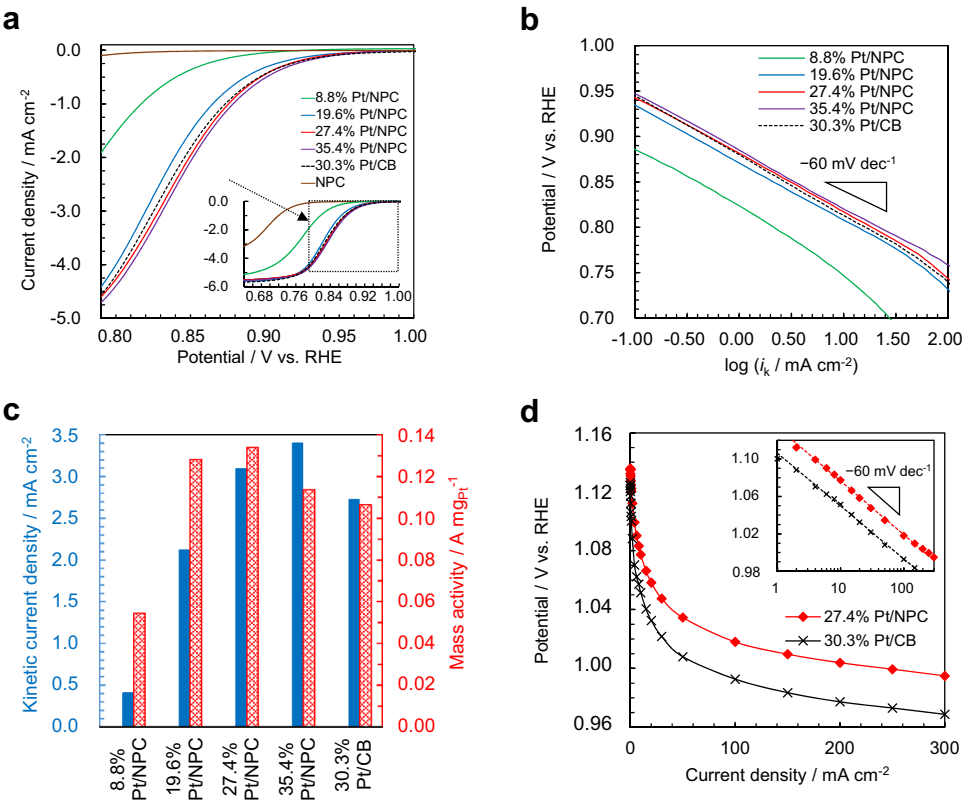

Fig. 5 **a** Voltammograms at a rotation rate of 1600 rpm of Pt/NPCs, 30.3% Pt/CB, and NPC. **b** Tafel plots obtained after correction of the RDE data for O_2 diffusion and **c** kinetic current density and mass activity at 0.85 V for Pt/NPCs and 30.3% Pt/CB. **d** Polarization curves of GDEs using 27.4% Pt/NPC and 30.3% Pt/CB. The inset of **d** shows Tafel plots based on the polarization curves

the nanostructure. Moreover, the particles appear to be porous, which is advantageous for their application in fuel cells and metal–air batteries [74, 75]. The primary particles form agglomerates, and mesopores are present between the particles within the agglomerates. Furthermore, the agglomerates form chain-like aggregates, creating both an extensive network of meso- and macropores and continuous electronic conducting pathways (schematic illustration shown in Fig. S5). The N_2 adsorption/desorption isotherms and BJH pore size distributions for the Pt/NPCs, NPC, 30.3% Pt/CB, and CB are shown in Figs. 4 and S6. The BET surface area, total pore volumes, and micropore volumes are summarized in Table S1. The isotherm of the NPC displays a distinct hysteresis loop over a wide partial pressure region ($P/P_0 > 0.42$), which is attributed to mesopores. Near a P/P_0 value of 1.0, no saturation was observed, indicating the presence of macropores. Although the adsorption volume per mass was reduced along with increasing weight percentage of Pt, the characteristic shapes of isotherms were also obtained for all Pt/NPCs.

3.2 Electrocatalytic properties of Pt nanoparticles supported on nitrogen-doped porous carbon

To evaluate the electrocatalytic activity of the synthesized catalysts for the ORR, RDE measurements were conducted in O_2-saturated 0.1 M KOH solution. Voltammograms for the Pt/NPCs and 30.3% Pt/CB show a single reduction wave with a mixed kinetic-diffusion control region, about $0.71\ V < E < 0.95\ V$, above a flat diffusion-limited current density plateau at approximately $-5.7\ mA\ cm^{-2}$ (Fig. 5a). The current density value is consistent with the four-electron limiting current for the ORR, which was previously reported for a platinum single-crystalline electrode [76] and corresponds to a theoretical value calculated using the Levich equation, suggesting a negligible contribution from O_2 diffusion through the Nafion binder [57, 77]. In order to quantitatively determine the ORR pathway, rotating ring disk electrode measurements were further performed (Fig. S7). The number of electrons transferred was approximately four, and almost no hydrogen peroxide formation was observed for the Pt/NPCs and 30.3% Pt/CB in the potential region above 0.57 V.

Figure 5b shows Tafel plots of the RDEs for synthesized catalysts. The slopes were −69.7, −62.0, −63.8, −59.2, and $-62.6\ mV\ decade^{-1}$ for 8.8% Pt/NPC, 19.6% Pt/NPC, 27.4% Pt/NPC, 35.4% Pt/NPC, and 30.3% Pt/CB, respectively. The slope values of approximately $-60\ mV\ decade^{-1}$ for the Pt/NPCs (excluding 8.8% Pt/NPC) and 30.3% Pt/CB would be ascribed to Temkin adsorption, in which coverage of oxygen species, such as OH and O, on the Pt surface was high [78, 79]. OH would be the main oxygen species in alkaline solution [80]. The kinetic current density and mass

activity of the Pt/NPCs and 30.3% Pt/CB are compared in Fig. 5c. 19.6% Pt/NPC and 27.4% Pt/NPC show high mass activity in the synthesized catalysts. The mass activity for the 27.4% Pt/NPC at 0.85 V is 0.13 A mg_{Pt}^{-1}, which is lower than 0.38 A mg_{Pt}^{-1} for 8.06% hydrogenated Pt/$CaMnO_3$ (mean size: 1.0 nm) [81], but it is higher than 0.028 A mg_{Pt}^{-1} for 12.9% Pt/nitrogen-doped graphene (mean size: 6.2 nm, nitrogen concentration: ~ 5 wt.%) [82] and 0.075 A mg_{Pt}^{-1} for commercial 10% Pt/C (Johnson Matthey) [81].

To investigate the usage of synthesized Pt/NPC, 27.4% Pt/NPC was used as an ORR catalyst in a GDE; GDEs have been utilized as oxygen electrodes in fuel cells and metal–air batteries [74, 75]. Figure 5d shows steady-state polarization curves for GDEs using 27.4% Pt/NPC and 30.3% Pt/CB. The kinetic activity cannot be directly read from the *i*R-corrected plots for GDEs, at high current densities where mass transport effects are significant, whereas at lower current densities the cathode reaction kinetics become more dominant in determining the GDE performance [74, 83]. No obvious potential drop was observed in the measured current density in the Tafel plot of 27.4% Pt/NPC, suggesting that the plot shape is kinetically controlled (Fig. 5d inset). Moreover, the slope values of the Tafel plots were approximately – 60 mV $decade^{-1}$ (– 59.3 and – 57.5 mV $decade^{-1}$ for 27.4% Pt/NPC and 30.3% Pt/CB), consistent with the RDE results. In GDEs for alkaline fuel cells and metal–air batteries, oxygen molecule is reduced to hydroxide at the three-phase boundary between gas, the alkaline solution, and the solid catalyst [74]. For optimal utilization of the three-phase boundary, meso- and macroporous structures of support materials are particularly important because the large pores can provide effective paths of mass transfer in the catalyst layer [84, 85]. Thus, the high meso- and macropore volumes, which constitute 89% of the total pore volume (Table S1), as well as good electronic conducting pathways in the porous structure of 27.4% Pt/NPC would be favorable for use in a GDE. In particular, at high current densities, not only the high catalytic activity for the ORR but also the porous structure of 27.4% Pt/NPC may contribute to its superior electrode performance. For comparison, the potentials of GDEs at current densities of 100 and 250 mA cm^{-2} are summarized in Table S2. In terms of the potentials, the performance of the GDE using 27.4% Pt/NPC is superior than that of a previously reported GDE using commercial Pt/C (TEC 10A30E, Tanaka Kikinzoku Kogyo) installed in a PTFE-made cell, which was also used in the present study [62], and other GDEs in alkaline solutions.

We further compared the specific activity and summarized the electrochemical results for the synthesized catalysts in Fig. 6a and Table S3. A correlation was observed between the mean particle size and the activity of the Pt/NPCs, although 30.3% Pt/CB with larger mean particle

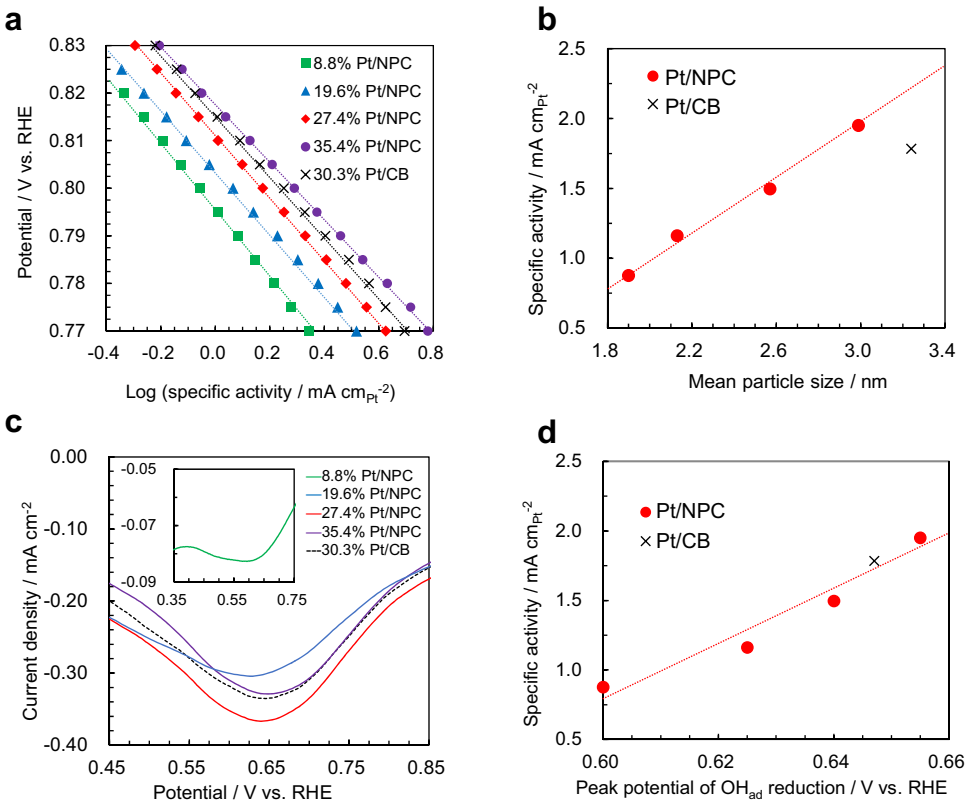

Fig. 6 **a** Potential with respect to specific activity of Pt/NPCs and 30.3% Pt/CB. For the plots, the Tafel plots on RDE (Fig. 5b) were replotted. The specific activity was calculated by normalizing the kinetic current to the electrochemical surface area (Fig. S8). **b** Correlation between the specific activity at 0.80 V and the mean particle size of Pt/NPCs and 30.3% Pt/CB. **c** Voltammograms of Pt/NPCs and 30.3% Pt/CB in N_2-saturated 0.1 M KOH solution. **d** Dependence of the specific activity at 0.80 V to the peak potential of OH_{ad} reduction for Pt/NPCs and 30.3% Pt/CB

size exhibits lower specific activity than 35.4% Pt/NPC with mean particle size of 2.99 nm (Fig. 6b). Figure 6c and d show peaks associated with the reduction of the adsorbed OH (OH_{ad}) on the Pt nanoparticles and the dependence of the specific activity on the peak potential for the synthesized catalysts, respectively. The potential is a good indicator of the adsorption strength of oxygen species, which inhibit adsorption of molecular O_2, on Pt [86–88]. Lower potentials for Pt/NPCs with smaller mean particle sizes would indicate stronger adsorption of the species. Therefore, the lower specific activity of Pt/NPCs with smaller mean particle sizes would be attributed to the stronger adsorption of the oxygen species on the nanoparticles. Mayrhofer et al. found a similar negative shift of OH_{ad} reduction peaks with decreasing particle size, as one may expect for flatter surfaces and a decreasing average atomic coordination number [21]. Thus, the decrease in the specific activity of Pt/NPC with smaller mean particle sizes could be attributed to the decrease in the average coordination number. Notably, 35.4% Pt/NPC with small mean particle size of 2.99 nm exhibits a slightly high peak potential of OH_{ad} reduction and improved activity compared with 30.3% Pt/CB (mean particle size: 3.24 nm). Pt nanoparticles supported on nitrogen-doped carbon are typically prepared via deposition of the nanoparticles from platinum salts [89]. In the synthesis, Pt nanoparticles would nucleate and grow on the nitrogen atoms, where the Pt nanoparticles and nitrogen-doped carbon support can strongly interact [45, 65]. A positive shift of the binding energy for Pt 4*f* in the XPS spectra of the Pt/NPCs would reflect a modified electronic structure of Pt by NPC support, which can decrease the adsorption strength of detrimental oxygen species, such as OH and CO, on Pt [68]. Thus, the decrease in the adsorbate–Pt strength might enhance the specific activity of Pt nanoparticles supported on NPC. Although a detailed mechanism that underlies the enhancement has to be studied further, the present study demonstrates an efficient structure that could guide the design of improved catalysts using Pt nanoparticles and NPC.

4 Conclusions

Pt nanoparticles supported on highly porous nitrogen-doped carbon were prepared via a simple alcohol reduction method. Pt nanoparticles with mean size in the range from 1.90 to 2.99 nm were uniformly deposited on NPC support with loadings of 8.8–35.4 wt.%. The increased number of nucleation sites provided by nitrogen atoms would contribute to the deposition of small nanoparticles. Pt 4*f* XPS spectra showed a positive shift of the binding energy, suggesting the presence of strong interactions between the Pt nanoparticles and NPC. Although 8.8% Pt/NPC with too small particle size exhibited low mass activity for the ORR, the Pt/NPCs (excluding 8.8% Pt/NPC) showed superior mass activity compared with 30.3% Pt/CB. When used as an ORR catalyst in the construction of a GDE, 27.4% Pt/NPC with high catalytic activity and hierarchical pore structure exhibited no obvious potential drop in its Tafel plot. The specific activity for the ORR of the Pt/NPCs and 30.3% Pt/CB correlated with the peak potential of OH_{ad} reduction, reflecting the adsorption strength of oxygen species on Pt, which was dependent on the mean particle size and support.

Acknowledgements This work was partially supported by the Japan Society for the Promotion of Science (JSPS) Grants-in-Aid for Scientific Research (KAKENHI) Grant Number JP 20K15223.

Compliance with ethical standards

Conflict of interest The authors declare that they have no conflict of interest.

References

1. Bidault F, Brett DJL, Middleton PH et al (2010) An improved cathode for alkaline fuel cells. Int J Hydrogen Energy 35:1783–1788. https://doi.org/10.1016/j.ijhydene.2009.12.035
2. Wagner N, Schulze M, Gülzow E (2004) Long term investigations of silver cathodes for alkaline fuel cells. J Power Sources 127:264–272. https://doi.org/10.1016/j.jpowsour.2003.09.022
3. Sarapuu A, Kibena-Põldsepp E, Borghei M, Tammeveski K (2018) Electrocatalysis of oxygen reduction on heteroatom-doped nanocarbons and transition metal-nitrogen-carbon catalysts for alkaline membrane fuel cells. J Mater Chem A 6:776–804. https://doi.org/10.1039/c7ta08690c
4. He Q, Cairns EJ (2015) Review—recent progress in electrocatalysts for oxygen reduction suitable for alkaline anion exchange membrane fuel cells. J Electrochem Soc 162:F1504–F1539. https://doi.org/10.1149/2.0551514jes
5. Liu Q, Pan Z, Wang E et al (2020) Aqueous metal-air batteries: fundamentals and applications. Energy Storage Mater 27:478–505. https://doi.org/10.1016/j.ensm.2019.12.011
6. Wittmaier D, Danner T, Wagner N, Friedrich KA (2014) Screening and further investigations on promising bi-functional

catalysts for metal-air batteries with an aqueous alkaline electrolyte. J Appl Electrochem 44:73–85. https://doi.org/10.1007/s10800-013-0602-x
7. Chatenet M, Aurousseau M, Durand R, Andolfatto F (2003) Silver-platinum bimetallic catalysts for oxygen cathodes in chlor-alkali electrolysis: comparison with pure platinum. J Electrochem Soc 150:D47–D55. https://doi.org/10.1149/1.1540063
8. Li X, Popov BN, Kawahara T, Yanagi H (2011) Non-precious metal catalysts synthesized from precursors of carbon, nitrogen, and transition metal for oxygen reduction in alkaline fuel cells. J Power Sources 196:1717–1722. https://doi.org/10.1016/j.jpowsour.2010.10.018
9. Dekel DR (2018) Review of cell performance in anion exchange membrane fuel cells. J Power Sources 375:158–169. https://doi.org/10.1016/j.jpowsour.2017.07.117
10. Wang YJ, Zhao N, Fang B et al (2015) Carbon-supported pt-based alloy electrocatalysts for the oxygen reduction reaction in polymer electrolyte membrane fuel cells: particle size, shape, and composition manipulation and their impact to activity. Chem Rev 115:3433–3467. https://doi.org/10.1021/cr500519c
11. Hussain S, Erikson H, Kongi N et al (2020) Oxygen reduction reaction on nanostructured Pt-based electrocatalysts: a review. Int J Hydrogen Energy 45:31775–31797. https://doi.org/10.1016/j.ijhydene.2020.08.215
12. Fang B, Chaudhari NK, Kim M-S et al (2009) Homogeneous deposition of platinum nanoparticles on carbon black for proton exchange membrane fuel cell. J Am Chem Soc 131:15330–15338. https://doi.org/10.1021/ja905749e
13. Nie Y, Li L, Wei Z (2015) Recent advancements in Pt and Pt-free catalysts for oxygen reduction reaction. Chem Soc Rev 44:2168–2201. https://doi.org/10.1039/c4cs00484a
14. Zhong C-J, Luo J, Fang B et al (2010) Nanostructured catalysts in fuel cells. Nanotechnology 21:062001. https://doi.org/10.1088/0957-4484/21/6/062001
15. Kinoshita K (1990) Particle size effects for oxygen reduction on highly dispersed platinum in acid electrolytes. J Electrochem Soc 137:845–848. https://doi.org/10.1149/1.2086566
16. Peuckert M, Yoneda T, Betta RAD, Boudart M (1986) Oxygen reduction on small supported platinum particles. J Electrochem Soc 133:944–947. https://doi.org/10.1149/1.2108769
17. Perez J, Gonzalez ER, Ticianelli EA (1998) Oxygen electrocatalysis on thin porous coating rotating platinum electrodes. Electrochim Acta 44:1329–1339. https://doi.org/10.1016/S0013-4686(98)00255-2
18. Romanowski W (1969) Equilibrium forms of very small metallic crystals. Surf Sci 18:373–388. https://doi.org/10.1016/0039-6028(69)90180-0
19. Katsounaros I, Cherevko S, Zeradjanin AR, Mayrhofer KJJ (2014) Oxygen electrochemistry as a cornerstone for sustainable energy conversion. Angew Chemie Int Ed 53:102–121. https://doi.org/10.1002/anie.201306588
20. Han BC, Miranda CR, Ceder G (2008) Effect of particle size and surface structure on adsorption of O and OH on platinum nanoparticles: a first-principles study. Phys Rev B 77:1–9. https://doi.org/10.1103/PhysRevB.77.075410
21. Mayrhofer KJJ, Blizanac BB, Arenz M et al (2005) The impact of geometric and surface electronic properties of Pt-catalysts on the particle size effect in electrocatalysis. J Phys Chem B 109:14433–14440. https://doi.org/10.1021/jp051735z
22. Markoví NM, Ross PN (2002) Surface science studies of model fuel cell electrocatalysts. Surf Sci Rep 45:117–229. https://doi.org/10.1016/s0167-5729(01)00022-x
23. Tammeveski K, Arulepp M, Tenno T et al (1997) Oxygen electroreduction on titanium-supported thin Pt films in alkaline solution. Electrochim Acta 42:2961–2967. https://doi.org/10.1016/S0013-4686(97)00119-9
24. Tammeveski K, Tenno T, Claret J, Ferrater C (1997) Electrochemical reduction of oxygen on thin-film Pt electrodes in 0.1 M KOH. Electrochim Acta 42:893–897. https://doi.org/10.1016/S0013-4686(96)00325-8
25. Watanabe M, Sei H, Stonehart P (1989) The influence of platinum crystallite size on the electroreduction of oxygen. J Electroanal Chem 261:375–387. https://doi.org/10.1016/0022-0728(89)85006-5
26. Antolini E (2016) Structural parameters of supported fuel cell catalysts: the effect of particle size, inter-particle distance and metal loading on catalytic activity and fuel cell performance. Appl Catal B Environ 181:298–313. https://doi.org/10.1016/j.apcatb.2015.08.007
27. Sharma S, Pollet BG (2012) Support materials for PEMFC and DMFC electrocatalysts - a review. J Power Sources 208:96–119. https://doi.org/10.1016/j.jpowsour.2012.02.011
28. Wang YJ, Wilkinson DP, Zhang J (2011) Noncarbon support materials for polymer electrolyte membrane fuel cell electrocatalysts. Chem Rev 111:7625–7651. https://doi.org/10.1021/cr100060r
29. Ahmadi M, Mistry H, Roldan Cuenya B (2016) Tailoring the catalytic properties of metal nanoparticles via support interactions. J Phys Chem Lett 7:3519–3533. https://doi.org/10.1021/acs.jpclett.6b01198
30. Li Y, Gao W, Ci L et al (2010) Catalytic performance of Pt nanoparticles on reduced graphene oxide for methanol electro-oxidation. Carbon 48:1124–1130. https://doi.org/10.1016/j.carbon.2009.11.034
31. Kabir S, Serov A, Artyushkova K, Atanassov P (2016) Design of novel graphene materials as a support for palladium nanoparticles: highly active catalysts towards ethanol electrooxidation. Electrochim Acta 203:144–153. https://doi.org/10.1016/j.electacta.2016.04.026
32. Chien CC, Jeng KT (2006) Effective preparation of carbon nanotube-supported Pt-Ru electrocatalysts. Mater Chem Phys 99:80–87. https://doi.org/10.1016/j.matchemphys.2005.09.080
33. Bittencourt C, Hecq M, Felten A et al (2008) Platinum-carbon nanotube interaction. Chem Phys Lett 462:260–264. https://doi.org/10.1016/j.cplett.2008.07.082
34. Li Y, Wang F, Zhu H (2020) Synthesis of H_2O_2–CTAB dual-modified carbon black-supported Pt_3Ni to improve catalytic activity for ORR. J Mater Sci 55:11241–11252. https://doi.org/10.1007/s10853-020-04808-y
35. Hara M, Lee M, Liu CH et al (2012) Electrochemical and Raman spectroscopic evaluation of Pt/graphitized carbon black catalyst durability for the start/stop operating condition of polymer electrolyte fuel cells. Electrochim Acta 70:171–181. https://doi.org/10.1016/j.electacta.2012.03.043
36. Honji A, Marl T, Hishinuma Y, Kurita K (1988) Platinum supported on silicon carbide as fuel cell electrocatalyst. J Electrochem Soc 135:917–918. https://doi.org/10.1149/1.2095831
37. Hara Y, Minami N, Matsumoto H, Itagaki H (2007) New synthesis of tungsten carbide particles and the synergistic effect with Pt metal as a hydrogen oxidation catalyst for fuel cell applications. Appl Catal A Gen 332:289–296. https://doi.org/10.1016/j.apcata.2007.08.030
38. Ioroi T, Siroma Z, Fujiwara N et al (2005) Sub-stoichiometric titanium oxide-supported platinum electrocatalyst for polymer electrolyte fuel cells. Electrochem commun 7:183–188. https://doi.org/10.1016/j.elecom.2004.12.007
39. Stambula S, Gauquelin N, Bugnet M et al (2014) Chemical structure of nitrogen-doped graphene with single platinum atoms and atomic clusters as a platform for the PEMFC electrode. J Phys Chem C 118:3890–3900. https://doi.org/10.1021/jp408979h
40. Ye S, Vijh AK, Dao LH (1997) A new fuel cell electrocatalyst based on carbonized polyacrylonitrile foam: the nature of

platinum-support interactions. J Electrochem Soc 144:90–95. https://doi.org/10.1149/1.1837369
41. Xiong B, Zhou Y, Zhao Y et al (2013) The use of nitrogen-doped graphene supporting Pt nanoparticles as a catalyst for methanol electrocatalytic oxidation. Carbon 52:181–192. https://doi.org/10.1016/j.carbon.2012.09.019
42. Lepró X, Terrés E, Vega-Cantú Y et al (2008) Efficient anchorage of Pt clusters on N-doped carbon nanotubes and their catalytic activity. Chem Phys Lett 463:124–129. https://doi.org/10.1016/j.cplett.2008.08.001
43. Jukk K, Kongi N, Rauwel P et al (2016) Platinum nanoparticles supported on nitrogen-doped graphene nanosheets as electrocatalysts for oxygen reduction reaction. Electrocatalysis 7:428–440. https://doi.org/10.1007/s12678-016-0322-1
44. Sun C-L, Chen L-C, Su M-C et al (2005) Ultrafine platinum nanoparticles uniformly dispersed on arrayed cn_x nanotubes with high electrochemical activity. Chem Mater 17:3749–3753. https://doi.org/10.1021/cm050107r
45. Zhou Y, Neyerlin K, Olson TS et al (2010) Enhancement of Pt and Pt-alloy fuel cell catalyst activity and durability via nitrogen-modified carbon supports. Energy Environ Sci 3:1437–1446. https://doi.org/10.1039/c003710a
46. Tachibana N, Ikeda S, Yukawa Y, Kawaguchi M (2017) Highly porous nitrogen-doped carbon nanoparticles synthesized via simple thermal treatment and their electrocatalytic activity for oxygen reduction reaction. Carbon 115:515–525. https://doi.org/10.1016/j.carbon.2017.01.034
47. Spinacé EV, Linardi M, Neto AO (2005) Co-catalytic effect of nickel in the electro-oxidation of ethanol on binary Pt-Sn electrocatalysts. Electrochem commun 7:365–369. https://doi.org/10.1016/j.elecom.2005.02.006
48. Neto AO, Dias RR, Tusi MM et al (2007) Electro-oxidation of methanol and ethanol using PtRu/C, PtSn/C and PtSnRu/C electrocatalysts prepared by an alcohol-reduction process. J Power Sources 166:87–91. https://doi.org/10.1016/j.jpowsour.2006.12.088
49. Antolini E, Giorgi L, Cardellini F, Passalacqua E (2001) Physical and morphological characteristics and electrochemical behaviour in PEM fuel cells of PtRu/C catalysts. J Solid State Electrochem 5:131–140. https://doi.org/10.1007/s100080000116
50. Wang H, Maiyalagan T, Wang X (2012) Review on recent progress in nitrogen-doped graphene: Synthesis, characterization, and its potential applications. ACS Catal 2:781–794. https://doi.org/10.1021/cs200652y
51. An H, An GH, Ahn HJ (2015) Octahedral Co_3O_4/carbon nanofiber composite-supported Pt catalysts for improved methanol electrooxidation. J Alloys Compd 645:317–321. https://doi.org/10.1016/j.jallcom.2015.05.105
52. Rao CV, Parrondo J, Ghatty SL, Rambabu B (2010) High temperature polymer electrolyte membrane fuel cell performance of Pt_xCo_y/C cathodes. J Power Sources 195:3425–3430. https://doi.org/10.1016/j.jpowsour.2009.12.022
53. Barrett EP, Joyner LG, Halenda PP (1951) The determination of pore volume and area distributions in porous substances. I. computations from nitrogen isotherms. J Am Chem Soc 73:373–380. https://doi.org/10.1021/ja01145a126
54. Brunauer S, Emmett PH, Teller E (1938) Adsorption of gases in multimolecular layers. J Am Chem Soc 60:309–319. https://doi.org/10.1021/ja01269a023
55. de Boer JH, Lippens BC, Linsen BG et al (1966) The t-curve of multimolecular N_2-adsorption. J Colloid Interface Sci 21:405–414. https://doi.org/10.1016/0095-8522(66)90006-7
56. Kruk M, Jaroniec M (2001) Gas adsorption characterization of ordered organic-inorganic nanocomposite materials. Chem Mater 13:3169–3183. https://doi.org/10.1021/cm0101069
57. Garsany Y, Baturina OA, Swider-Lyons KE, Kocha SS (2010) Experimental methods for quantifying the activity of platinum electrocatalysts for the oxygen reduction reaction. Anal Chem 82:6321–6328. https://doi.org/10.1021/ac100306c
58. Bard A, Faulkner L (2000) Electrochemical methods: fundamentals and applications, 2nd edn. Wiley, New York
59. Pozio A, De Francesco M, Cemmi A et al (2002) Comparison of high surface Pt/C catalysts by cyclic voltammetry. J Power Sources 105:13–19. https://doi.org/10.1016/S0378-7753(01)00921-1
60. Vidal-Iglesias FJ, Arán-Ais RM, Solla-Gullón J et al (2012) Electrochemical characterization of shape-controlled Pt nanoparticles in different supporting electrolytes. ACS Catal 2:901–910. https://doi.org/10.1021/cs200681x
61. Geniès L, Faure R, Durand R (1998) Electrochemical reduction of oxygen on platinum nanoparticles in alkaline media. Electrochim Acta 44:1317–1327. https://doi.org/10.1016/S0013-4686(98)00254-0
62. Yuasa M, Tachibana N, Shimanoe K (2013) Oxygen reduction activity of carbon-supported $La_{1-x}Ca_xMn_{1-y}Fe_yO_3$ nanoparticles. Chem Mater 25:3072–3079. https://doi.org/10.1021/cm401276y
63. Cheng Y, Lu H, Zhang K et al (2018) Fabricating Pt-decorated three dimensional N-doped carbon porous microspherical cavity catalyst for advanced oxygen reduction reaction. Carbon 128:38–45. https://doi.org/10.1016/j.carbon.2017.10.102
64. Szabó T, Berkesi O, Forgó P et al (2006) Evolution of surface functional groups in a series of progressively oxidized graphite oxides. Chem Mater 18:2740–2749. https://doi.org/10.1021/cm060258+
65. Li Y-H, Hung T-H, Chen C-W (2009) A first-principles study of nitrogen- and boron-assisted platinum adsorption on carbon nanotubes. Carbon 47:850–855. https://doi.org/10.1016/j.carbon.2008.11.048
66. Long G-F, Li X-H, Wan K et al (2017) $Pt/C_{N\text{-doped}}$ electrocatalysts: Superior electrocatalytic activity for methanol oxidation reaction and mechanistic insight into interfacial enhancement. Appl Catal B Environ 203:541–548. https://doi.org/10.1016/j.apcatb.2016.10.055
67. Banis MN, Sun S, Meng X et al (2013) $TiSi_2O_x$ coated N-doped carbon nanotubes as Pt catalyst support for the oxygen reduction reaction in PEMFCs. J Phys Chem C 117:15457–15467. https://doi.org/10.1021/jp3118874,80
68. Zhu J, Xiao M, Zhao X et al (2015) Strongly coupled Pt nanotubes/N-doped graphene as highly active and durable electrocatalysts for oxygen reduction reaction. Nano Energy 13:318–326. https://doi.org/10.1016/j.nanoen.2015.03.002
69. Holme T, Zhou Y, Pasquarelli R, O'Hayre R (2010) First principles study of doped carbon supports for enhanced platinum catalysts. Phys Chem Chem Phys 12:9461–9468. https://doi.org/10.1039/b927263a
70. Melke J, Peter B, Habereder A et al (2016) Metal-support interactions of platinum nanoparticles decorated N-doped carbon nanofibers for the oxygen reduction reaction. ACS Appl Mater Interfaces 8:82–90. https://doi.org/10.1021/acsami.5b06225
71. Trusovas R, Račiukaitis G, Niaura G et al (2016) Recent advances in laser utilization in the chemical modification of graphene oxide and its applications. Adv Opt Mater 4:37–65. https://doi.org/10.1002/adom.201500469
72. Wu G, Johnston CM, Mack NH et al (2011) Synthesis-structure-performance correlation for polyaniline-Me-C non-precious metal cathode catalysts for oxygen reduction in fuel cells. J Mater Chem 21:11392–11405. https://doi.org/10.1039/c0jm03613g
73. Zhu M, Weber CJ, Yang Y et al (2008) Chemical and electrochemical ageing of carbon materials used in supercapacitor

electrodes. Carbon 46:1829–1840. https://doi.org/10.1016/j.carbon.2008.07.025
74. Bidault F, Brett DJL, Middleton PH, Brandon NP (2009) Review of gas diffusion cathodes for alkaline fuel cells. J Power Sources 187:39–48. https://doi.org/10.1016/j.jpowsour.2008.10.106
75. Danner T, Eswara S, Schulz VP, Latz A (2016) Characterization of gas diffusion electrodes for metal-air batteries. J Power Sources 324:646–656. https://doi.org/10.1016/j.jpowsour.2016.05.108
76. Markovic NM, Gasteiger HA, Ross PN (1996) Oxygen reduction on platinum low-index single-crystal surfaces in alkaline solution: rotating ring disk Pt(hkl) studies. J Phys Chem 100:6715–6721. https://doi.org/10.1021/jp9533382
77. Higuchi E, Uchida H, Watanabe M (2005) Effect of loading level in platinum-dispersed carbon black electrocatalysts on oxygen reduction activity evaluated by rotating disk electrode. J Electroanal Chem 583:69–76. https://doi.org/10.1016/j.jelechem.2005.01.041
78. Spendelow JS, Wieckowski A (2007) Electrocatalysis of oxygen reduction and small alcohol oxidation in alkaline media. Phys Chem Chem Phys 9:2654–2675. https://doi.org/10.1039/b703315j
79. Vinayan BP, Ramaprabhu S (2013) Platinum-TM (TM = Fe, Co) alloy nanoparticles dispersed nitrogen doped (reduced graphene oxide-multiwalled carbon nanotube) hybrid structure cathode electrocatalysts for high performance PEMFC applications. Nanoscale 5:5109–5118. https://doi.org/10.1039/c3nr00585b
80. Liu S, White MG, Liu P (2016) Mechanism of oxygen reduction reaction on Pt(111) in alkaline solution: importance of chemisorbed water on surface. J Phys Chem C 120:15288–15298. https://doi.org/10.1021/acs.jpcc.6b05126
81. Han X, Cheng F, Zhang T et al (2014) Hydrogenated uniform Pt clusters supported on porous $CaMnO_3$ as a bifunctional electrocatalyst for enhanced oxygen reduction and evolution. Adv Mater 26:2047–2051. https://doi.org/10.1002/adma.201304867
82. Varga T, Varga ÁT, Ballai G et al (2018) One step synthesis of chlorine-free Pt/Nitrogen-doped graphene composite for oxygen reduction reaction. Carbon 133:90–100. https://doi.org/10.1016/j.carbon.2018.03.020
83. Prasanna M, Ha HY, Cho EA et al (2004) Influence of cathode gas diffusion media on the performance of the PEMFCs. J Power Sources 131:147–154. https://doi.org/10.1016/j.jpowsour.2004.01.030
84. Eom SW, Lee CW, Yun MS, Sun YK (2006) The roles and electrochemical characterizations of activated carbon in zinc air battery cathodes. Electrochim Acta 52:1592–1595. https://doi.org/10.1016/j.electacta.2006.02.067
85. Okuda R, Nakano K, Suematsu K et al (2021) Chemical activation of nitrogen-doped carbon derived from chitosan with $ZnCl_2$ to produce a high-performance gas diffusion-type oxygen electrode. Electrochemistry 89:36–42. https://doi.org/10.5796/electrochemistry.20-00121
86. Shao M, Peles A, Shoemaker K (2011) Electrocatalysis on platinum nanoparticles: particle size effect on oxygen reduction reaction activity. Nano Lett 11:3714–3719. https://doi.org/10.1021/nl2017459
87. Kibsgaard J, Gorlin Y, Chen Z, Jaramillo TF (2012) Meso-structured platinum thin films: active and stable electrocatalysts for the oxygen reduction reaction. J Am Chem Soc 134:7758–7765. https://doi.org/10.1021/ja2120162
88. Markovic N, Gasteiger H, Ross PN (1997) Kinetics of oxygen reduction on Pt(hkl) electrodes: implications for the crystallite size effect with supported Pt electrocatalysts. J Electrochem Soc 144:1591–1597. https://doi.org/10.1149/1.1837646
89. Wang YJ, Fang B, Li H et al (2016) Progress in modified carbon support materials for Pt and Pt-alloy cathode catalysts in polymer electrolyte membrane fuel cells. Prog Mater Sci 82:445–498. https://doi.org/10.1016/j.pmatsci.2016.06.002